Original Article

JCBFM

Journal of Cerebral Blood Flow & Metabolism
2017, Vol. 37(11) 3599–3614

DOI: 10.1177/0271678X16685573
journals.sagepub.com/home/jcbfm
SAGE

Functional deficits induced by cortical microinfarcts

Philipp M Summers[1], David A Hartmann[1], Edward S Hui[2], Xingju Nie[3,4], Rachael L Deardorff[3,4], Emilie T McKinnon[3,4], Joseph A Helpern[1,3,4], Jens H Jensen[3,4] and Andy Y Shih[1,4]

Abstract

Clinical studies have revealed a strong link between increased burden of cerebral microinfarcts and risk for cognitive impairment. Since the sum of tissue damage incurred by microinfarcts is a miniscule percentage of total brain volume, we hypothesized that microinfarcts disrupt brain function beyond the injury site visible to histological or radiological examination. We tested this idea using a mouse model of microinfarcts, where single penetrating vessels that supply mouse cortex were occluded by targeted photothrombosis. We found that *in vivo* structural and diffusion MRI reliably reported the acute microinfarct core, based on spatial co-registrations with post-mortem stains of neuronal viability. Consistent with our hypothesis, c-Fos assays for neuronal activity and *in vivo* imaging of single vessel hemodynamics both reported functional deficits in viable peri-lesional tissues beyond the microinfarct core. We estimated that the volume of tissue with functional deficit in cortex was at least 12-fold greater than the volume of the microinfarct core. Impaired hemodynamic responses in peri-lesional tissues persisted at least 14 days, and were attributed to lasting deficits in neuronal circuitry or neurovascular coupling. These data show how individually miniscule microinfarcts could contribute to broader brain dysfunction during vascular cognitive impairment and dementia.

Keywords

Microinfarcts, microcirculation, neurovascular coupling, two-photon microscopy, vascular cognitive impairment

Received 31 May 2016; Revised 21 November 2016; Accepted 22 November 2016

Introduction

Overwhelming evidence has linked cerebrovascular disease to cognitive decline.[1,2] Microinfarcts, foci of neuronal loss that are ~0.05 to 3 mm in diameter, are believed to be an important factor in this linkage.[3–5] Collectively, post-mortem histological and *in vivo* radiological investigations have shown that microinfarct burden is greater in individuals with vascular cognitive impairment and dementia (VCID) compared to age-matched, non-demented controls.[4,6–10] Microinfarcts are thought to result from loss of blood flow through cerebral penetrating or perforating arterioles, as evidenced by preclinical studies that perturb small vessel flow,[11–14] and by a greater incidence of microinfarcts in individuals with cerebrovascular diseases such as atherosclerosis, arteriolosclerosis, and cerebral amyloid angiopathy (CAA).[15–17]

With an established link between microinfarcts and VCID, the field now seeks to identify the mechanisms by which such miniscule lesions could contribute to cognitive deficits. Recent studies have suggested that the observation of a few microinfarcts during neuropathology[18] or MRI[19] may correspond to hundreds, possibly thousands, that go undetected throughout the brain due to limited tissue sampling or low sensitivity during clinical imaging. However, a reportedly heavy burden of

[1]Department of Neurosciences, Medical University of South Carolina, Charleston, SC, USA
[2]Department of Diagnostic Radiology, The University of Hong Kong, Hong Kong
[3]Department of Radiology and Radiological Science, Medical University of South Carolina, Charleston, SC, USA
[4]Center for Biomedical Imaging, Medical University of South Carolina, Charleston, SC, USA

Corresponding author:
Andy Y Shih, Department of Neurosciences, Medical University of South Carolina, 173 Ashley Ave., CRI 406 Charleston, SC 29425, USA.
Email: shiha@musc.edu

average-sized microinfarcts (5000 spherical lesions of 1 mm diameter) sums to 2.6 mL of tissue lost to microinfarction. This generous estimate suggests that microinfarcts affect only 2% or less of the human brain volume, and does not appear to fully explain how microinfarcts could contribute to brain dysfunction. An important consideration is that this estimated tissue loss is based on the "core" of the microinfarct, a region of dead or dying tissue that exhibits pallor, neuronal loss, and microgliosis in routine histological stains.[20] We therefore hypothesized that microinfarcts could disrupt brain function beyond their nonviable cores.[4]

Although our understanding of the structural characteristics of microinfarcts has progressed, the functional impact of microinfarcts remains enigmatic for several reasons: (1) most microinfarcts are too small to be detected by clinical neuroimaging modalities,[21] (2) there is no means to assess functional impairments alongside measurements of tissue structure during postmortem examination of human tissues, and (3) microinfarcts occur in parallel with other disease factors, i.e. Alzheimer's disease, large-scale stroke, and aging, that cause brain dysfunction through mechanisms independent from microinfarcts.[6] To circumvent these issues, we examined the functionality of tissues surrounding single microinfarcts induced in the brains of normal adult mice. Microinfarcts were induced by selectively occluding single cortical penetrating arterioles through a cranial window using focal photothrombosis.[11,22] We then compared functional readouts of sensory-evoked brain activity, obtained by measuring activity-dependent c-Fos expression or *in vivo* two-photon imaging of single vessel hemodynamic responses, to the location of the microinfarct core. Our findings suggest that microinfarcts induce lasting functional impairments that extend well beyond the core, uncovering an invisible facet of microinfarct pathology that may contribute to the development of VCID.

Materials and methods

The Institutional Animal Care and Use Committee at the Medical University of South Carolina approved the procedures used in this study. The University has accreditation from the Association for Assessment and Accreditation of Laboratory Animal Care International, and all experiments were performed within its guidelines. All data were analyzed and reported according to ARRIVE guidelines.

Animals and surgery

Reagents were obtained from Sigma-Aldrich unless otherwise noted. We used male mice ranging three to six months of age for all experiments. Heterozygous CX3CR1$^{GFP/+}$ mice (bred on C57BL/6 background) were used in all MRI studies (Figures 1 to 3 and 8) (Jackson Laboratories #005582), which was useful for identification of resident microglia and infiltrating monocytes during histology. Heterozygous Thy1-YFP-H mice were used to visualize dendritic spines on layer 2/3 neurons (Figure 5) (Jackson Laboratories #003782). Pure C57BL/6 mice were used for data presented in all other figures (Jackson Laboratories #000664).

Animals were maintained in standard cages on a 12-h light-dark cycle and normal mouse chow diet. For cranial window and head-mount implantation, anesthesia was induced with isoflurane (Patterson Veterinary) at 4% mean alveolar concentration (MAC) in 100% oxygen and maintained at 1 to 2% MAC during surgery.[23] Body temperature was maintained at 37°C with a feedback-regulated heat pad (FHC). PoRTs windows were generated over the left cerebral hemisphere to gain optical access to the sensorimotor cortex,[23,24] under the guidance of a stereoscope (SXZ10; Olympus). An aluminum flange (or plastic flange for MRI studies) was cemented onto the contralateral hemisphere of the dorsal skull surface to enable head fixation during imaging. Buprenorphine was provided prior to the surgery at a concentration of 0.05 mg/kg for analgesia.

In vivo two-photon imaging

Imaging was performed with a Sutter Moveable Objective Microscope and a Coherent Ultra II Ti:Sapphire laser source. Our procedures for *in vivo* two-photon imaging have been described in detail previously.[22,23]

Since isoflurane dampens the hemodynamic response (Supplementary Figure 1),[25] studies of functionally evoked hemodynamics were performed on awake mice habituated to head-fixation, as previously described.[26] Mice were briefly anesthetized with 4% MAC isoflurane for an infraorbital vein injection of 2 MDa fluorescein-dextran (FD2000S; Sigma-Aldrich) prepared at a concentration of 5% (w/v) in sterile saline. They were then awoken and allowed to stabilize for 30 min prior to two-photon imaging. Movies encompassing 312 by 244 μm areas of the pial surface were collected at a frame rate of 4 Hz (800 nm excitation). The diameter of arterioles was quantified offline using full-width-at-half-maximum calculations of the fluorescence intensity profile across the vessel width.[26]

Whisker stimulation protocol

Whisker stimulation was performed while mice were awake and head-fixed under the microscope objective.[26] The stimulation protocol comprised air puffs (8 Hz, 20 ms pulse, 10 s pulse train, 35 p.s.i. from air tank) directed at

the mystacial pad contralateral to the hemisphere with the imaging window. The air was guided through a 200 μL plastic pipette tip (tip diameter = 2 mm) to focus the air stream on whisker rows B to D. The pipette tip was placed ~2 cm from the whiskers. A second air puffer was directed at the tail as a control for general arousal. Whisker and tail stimulation trials were presented in random order during the experiment. Ten trials of each stimulation type were collected for each imaged location. Each trial consisted of a 30 s baseline, 10 s stimulation, and 50 s post-stimulation period. Approximately 25 to 50% of the data was discarded due to motion artifacts that were detected by shifts from the imaging focal plane. Movement was also detected using an accelerometer (ADXL345; Sparkfun) mounted to the restraint tube. The signal from the accelerometer was amplified (DAM80, World Precision Instruments) and collected in an analog channel in parallel with movie data.

Targeted photothrombotic occlusions of single penetrating vessels

Focal photothrombotic occlusion of individual cortical penetrating arterioles or venules was described in detail previously.[22,27] For strategic placement of microinfarcts (Figures 4, 6, and 7), the primary barrel cortex was identified stereotaxically or with intrinsic optical imaging prior to photothrombosis.[11]

Magnetic resonance imaging

MRI was performed with a 7 T BioSpec 70/30 horizontal scanner (Bruker BioSpin) running Paravision 5.1 software and equipped with a 12 cm inner diameter actively shielded gradient system (440 mT/m). A quadrature volume coil (T128038) was used for signal transmission and a mouse brain array coil (T11765) for signal reception. Mice were maintained under 1.5% MAC isoflurane during image acquisition. An animal monitoring unit (SA instruments, Inc., model 1025) was used to record respiration and rectal temperature. Body temperature was maintained at 37°C using ventilated warm air, controlled by a feedback circuit between the heater and thermistor. Respiration was maintained between 50 and 70 breaths per minute during scanning. Detailed imaging parameters for each protocol are provided in Supplemental Materials.

MRI data analysis

The hyperintense regions in the inversion recovery (IR), T2-weighted, and averaged diffusion weighted images (b-value 2000 s/mm^2) were manually outlined using MRIcron software (Figures 2, 3, and 8). For Figure 8, the peri-lesional region of interest (ROI) surrounding the core was extended five voxels (780 μm) in all directions from the outermost edge of the microinfarct core. The peri-lesional ROI was drawn to avoid overlapping with neighboring microinfarcts, tissue boundaries, or apparent imaging artifacts. A circumferential boundary of one voxel width between the core and peri-lesional area (160 μm) was excluded to minimize partial volume effects. Both core and peri-lesional ROIs were drawn on the time-point with the largest lesion core (typically post-occlusion day 1 or 2). These same ROIs were then applied to all other time-points. Mean diffusivity and mean kurtosis (MK) values were calculated with diffusional kurtosis estimator (http://www.nitrc.org/projects/dke/).[28]

Immunohistology

For data of Figure 2, animals were sacrificed for histological examination at nine days post-occlusion. For data of Figure 3, animals were sacrificed at 24 h post-occlusion. All animals were perfusion fixed with 4% paraformaldehyde (PFA) in PBS through a transcardiac route.[22] After overnight fixation in 4% PFA in PBS, the whole brain was then mounted for vibratome sectioning such that it could be sliced tangential to the cortical surface at the location of the microinfarcts. Brain sections were collected at a thickness of 50 μm.

Immunostaining was performed as described previously,[22] with the following antibody combinations: (i) anti-NeuN primary antibody from guinea pig host (ABN90P; 1:1000 dilution; Millipore), followed by Alexa 594 secondary antibody (A11076, 1:1000 dilution; ThermoFisher) or DyLight 405 secondary antibody (106-475-003, 1:500 dilution; Jackson Immunoresearch), and (ii) anti-GFAP primary antibody from rabbit host (04-1062, 1:1000 dilution; Millipore) followed by Alexa 594 secondary antibody (A31632, 1:1000 dilution; ThermoFisher). Tissues were mounted on slides and briefly allowed to dry. The slides were then coverslip sealed with Fluoromount G. Fluorescence images were collected with an epi-fluorescence microscope (BX53; Olympus). Microinfarct areas were quantified from anti-NeuN stained tissue sections (Figure 3(c)). The microinfarct core was delineated as the border between normal tissue exhibiting dense neuronal nuclei and infarcted regions devoid of nuclei.

For c-Fos studies in Figure 4 and Supplementary Figure 2, mice received air puffs to the whiskers when awake as described above, but for a prolonged period of 20 min.[29] Mice were then sacrificed and perfusion fixed 75 min after stimulation. Cortices were flattened in order to visualize all barrels of layer 4 in a single slice. Brains were cut down the midline and the subcortical tissues (but not hippocampus) were carefully removed with forceps. The ventral 1/3 of the cortex was cut off so that the convex shape of the isolated cortex did not lead

to tissue distortion during the flattening process. The cortex was then flattened between two microscope slides, separated by 1.5 mm divider at either end of the slides. The slides were submerged in 4% PFA in PBS overnight. The post-fixed tissue was sliced into 50-μm thick sections parallel to the cortical surface using a vibratome. Consistent with minimal tissue stretching, the dimensions of major barrel columns such as C2 (150–200 μm in the minor axis and 300–350 μm in the major axis; Supplementary Figure 3) were consistent with the dimension of barrel columns measured in past studies in which mouse cortex was not flattened.[30]

Immunohistochemistry for c-Fos studies was performed with anti-c-Fos primary antibody from rabbit host (sc-52; 1:500 dilution; Santa Cruz Biotech), anti-NeuN primary antibody from mouse host (MAB339; 1:500; Millipore), and anti-VGlut2 primary antibody from guinea pig host (AF1042; 1:5,000 dilution; R&D Systems;). Secondary antibodies consisted of anti-rabbit Alexa 594 (A11076; 1:1,000 dilution; ThermoFisher), anti-guinea pig Alexa 488 (A31268; 1:1,000 dilution; ThermoFisher), and anti-mouse Alexa 350 (A21049: 1:1000 dilution; ThermoFisher). The ImageJ plugin ITCN (image-based tool for counting nuclei) was used to count c-Fos-positive or NeuN-positive cells from fluorescence images collected (Figure 4 and Supplementary Figures 2 and 4). Methods for analysis of synaptophysin immunostaining and dendritic spine density are provided in Supplemental Materials.

Statistical analysis

All statistical analyses were performed with MATLAB or Graphpad Prism software. Alpha-level for all tests was set a 0.05. Details for statistical outcomes can be found in the corresponding legend for each figure.

Experimental design

Animals were assigned to experimental groups with no bias and by different experimenters. Data analysis was not performed in a blinded fashion (except with spine counting), but results were not subjective since analysis protocols were largely automated, i.e. with Matlab or ImageJ code to calculate arteriole diameter or cell number. We did not perform tests to predetermine the sample size. Our sample size was similar to previously reported studies using related techniques.[11,22,26]

Results

Modeling microinfarcts in the mouse cortex

There is strong evidence that microinfarcts are a product of vascular obstruction at the level of small penetrating/perforating arterioles. In particular, the microinfarct core can harbor the remains of penetrating vessels with CAA[17] and possess histological features similar to larger ischemic insults.[31] We therefore modeled cortical microinfarcts in mice by generating localized obstructions in penetrating arterioles (Figure 1(a) to (c); red inset), or penetrating venules (not shown), under the guidance of *in vivo* two-photon microscopy.[11,22] Occlusions were made at the pial surface by forming localized clots in the target vessel lumen using focused photothrombotic irradiation.[11,22,32] It was possible to occlude two to three separate penetrating vessels in a $3 \times 3\,mm^2$ cranial window without causing microinfarcts to overlap in space.

Microinfarcts possessed T2-weighted signal contrast at 24 h post-onset (Figure 1(d)). They exhibited a roughly columnar shape and extended from the pial surface into the cortical gray matter, but rarely reached the underlying white matter of the external capsule. The shape, size, and location of these modeled cortical microinfarcts bore remarkable similarity to a subset of human microinfarcts captured in recent 7 T MRI studies (Figure 1(e))[33] and during neuropathological examination.[17,34,35] The similarity in microinfarct appearance between mouse and human is due to a relatively conserved cortical vascular scale between species, despite a large difference in brain size. That is, the mouse cortex is a ''cropped'' rather than ''scaled'' version of the human cortex. For example, the thickness of cerebral cortex is 1 to 2 mm for mice[36] and 2.8 to 3.5 mm for humans.[37] Penetrating arteriole irrigation territories span a ~0.5 to 1 mm in diameter across cortex in both mouse[30] and human.[38] This fortuitously allows for a straightforward comparison of the scale of microinfarct-induced functional deficits between species.

The evolution of MRI signals produced by microinfarcts

We next imaged mouse microinfarcts longitudinally with multiple MRI sequences, including T1-weighted, T2-weighted, IR, T2*-weighted, diffusion-weighted imaging (DWI), and diffusional kurtosis imaging (DKI)[39,40] (Figure 2). T2-weighted, IR, DWI, and DKI sequences revealed pronounced signal changes as microinfarct pathology evolved over nine days (Figure 2(a), and Supplementary Figures 5 and 6; green circles in left column show site of penetrating arteriole occlusion). T1-weighted imaging did not exhibit signal contrast with acute mouse microinfarcts (Supplementary Figure 5), unlike chronic human microinfarcts that often appear hypointense with T1.[33] Mouse microinfarcts also did not generate substantial change with a T2*-weighted sequence,

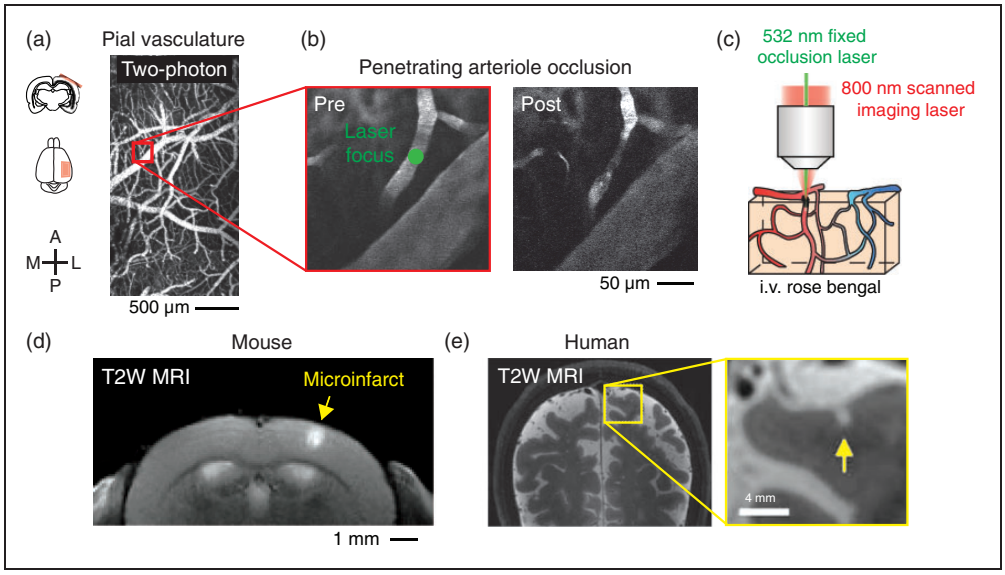

Figure 1. Modeling of microinfarcts in mice by optical occlusion of single cortical penetrating arterioles in vivo. (a) Wide-field two-photon imaging of the pial vasculature through a thinned-skull cranial window. A = anterior, L = lateral, P = posterior, M = medial. (b) High-resolution imaging and focal photothrombotic occlusion of a single penetrating arteriole. Green circle shows location of focused 532 nm laser irradiation. (c) Cartoon describing focal 532 nm laser activation of circulating Rose Bengal dye in targeted arterioles. Imaging is performed with an 800 nm scanned Ti-sapphire laser. (d) Coronal view of microinfarct resulting from occlusion of a single penetrating arteriole, viewed with T2-weighted 7 T MRI 24 h post-occlusion. (e) A cortical microinfarct identified in the living human brain using T2-weighted 7 T MRI. Data reproduced with permission from van Veluw et al.[33]

suggesting a lack of hemosiderin accumulation (Supplementary Figure 5).

To characterize the evolution of MRI signal change, we measured the area occupied by each microinfarct at various time-points after occlusion, focusing our analysis on T2-weighted, IR, and DKI sequences, which provided the most robust signals. In our analyses, we pooled data from arteriole and venular occlusions for the following reasons. First, MRI signals from arteriolar and venular microinfarcts evolved with a very similar timescale (Supplementary Figure 7). Second, we recently demonstrated that occlusion of a penetrating venule can indirectly affect flow in an upstream penetrating arteriole.[22] As a result, ischemic injury specific to arteriole flow loss is difficult to dissociate from venule flow since the networks are inherently connected. Third, it is conceivable that venule obstructions, caused for example by vein collagenosis or thrombosis, also contribute to the spectrum of microinfarcts in the human brain.

With all three imaging sequences, microinfarct area was found to peak between one to three days post-occlusion (Figure 2(b)). The visibility of microinfarcts then progressively decreased until becoming undetectable by five to nine days. Signal decrease was precipitous with IR imaging and microinfarcts were no longer visible by five days. T2-weighted imaging exhibited a slightly prolonged sensitivity out to seven days. Diffusion kurtosis imaging, which provides a measure of MK, had the greatest sensitivity, detecting microinfarcts up to nine days post-onset. Further, the duration of visibility with DKI was related to the size of the microinfarct (Figure 2(c)). That is, larger infarcts were visible for a longer duration of time, possibly due to a greater extent of edema and protracted inflammatory phases.

Mice were sacrificed for histology at nine days post-stroke to examine underlying tissue pathology (Figure 2(d)). This revealed the persistence of well-demarcated microinfarct cores, defined as a contiguous region devoid of staining for the neuronal nuclear protein, NeuN. The microinfarct core was laden with microglia/macrophages and surrounded by a broad ring of diffuse fibrillary gliosis. These features fit the descriptions of sub-acute microinfarcts in human neuropathological studies.[31]

Although optimized to occlude a single cortical arteriole at the brain surface, our photothrombotic method could potentially cause non-specific damage to underlying microvessels or brain tissue. To control for this possibility, we performed identical focal irradiations in regions distant from the neck of penetrating vessels, termed "off-target irradiations" (Figure 2(a); yellow circle in left column).[22] Overall, these off-target irradiations generated little to no MRI signal change (Figure 2(a)) and negligible tissue infarction

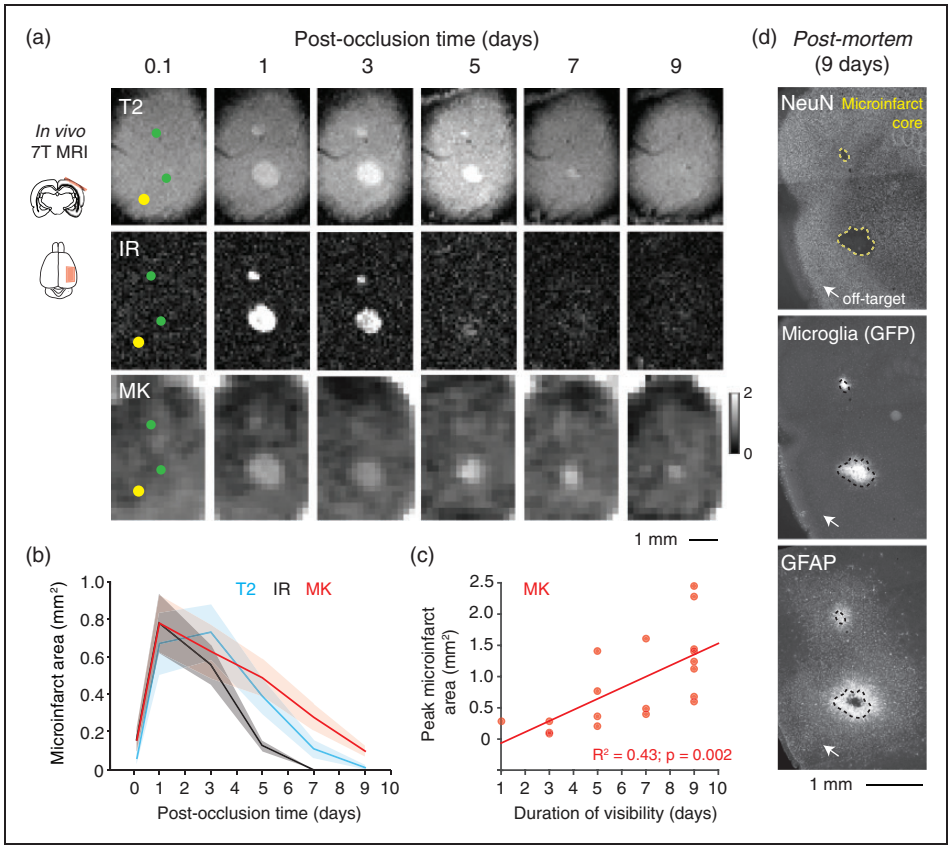

Figure 2. MRI signals associated with evolution of microinfarct pathology. (a) Longitudinal imaging of two microinfarcts using IR, T2 and DKI (MK) sequences. Lower green circle shows location of a penetrating arteriole occlusion. Upper green circle shows location of penetrating venule occlusion. Yellow circle is the location of a control off-target irradiation. (b) Area of microinfarcts plotted as function of post-occlusion time. We detected a statistically significant difference between imaging sequences ($p = 0.01$ main effect $F(2,38) = 5.2$; two-way ANOVA with repeated measures). Tukey post hoc analysis revealed differences between T2 versus IR at three days ($p = 0.003$) and five days ($p < 0.001$), MK versus T2 at seven days ($p = 0.003$), and MK and IR at five days ($p < 0.001$) and seven days ($p < 0.001$). Data are mean ± SEM. Panels b and c comprise data from n = 12 penetrating arteriole and n = 8 penetrating venule occlusions over seven mice. (c) Larger microinfarcts exhibit longer durations of visibility with DKI ($p = 0.002$, $R^2 = 0.43$, Pearson's correlation). (d) Post-mortem histology of mouse shown in panel (a). NeuN immunostaining shows the extent of the microinfarct core (yellow dotted line). GFP-labeled microglia intrinsic to the transgenic mouse used (CX3CR1-GFP$^{+/-}$) and GFAP immunostain show the extent of neuroinflammation in surrounding tissues.

(Figure 2(d)) (n = 3 for longitudinal imaging experiments). Thus, microinfarcts arose due to loss of blood flow in the perfusion domain of the targeted penetrating vessel, rather than off-target effects of the photothrombotic procedure.

MRI reports the nonviable core of acute microinfarcts

We next sought to understand what aspects of the microinfarct were detected by structural and diffusion MRI. One cohort of mice was sacrificed and perfusion fixed at 24 h post-occlusion, immediately following MRI scanning. Cortical tissues were sectioned in the same plane as MRI, i.e. tangential to the brain surface, allowing spatial registration between MRI and histology (Figure 3(a) to (c)). Over a broad range of microinfarct sizes, the regions of heightened IR signal and MK increase *in vivo* were strongly correlated with the histologically defined microinfarct core (Figure 3(d) and (e); red circles). DKI also seemed to report edematous tissues just beyond the microinfarct core, resulting in a ~1.25-fold increase in area compared to the true core (Figure 3(e); red circles). Off-target irradiations led to minimal MRI signal change and tissue infarction at the 24-h post-occlusion time-point (Figure 3(d) and (e); green circles). Thus, structural and diffusion sequences primarily report the nonviable core of acute microinfarcts. Accordingly, the viable tissues surrounding the microinfarct core were termed "peri-lesional."

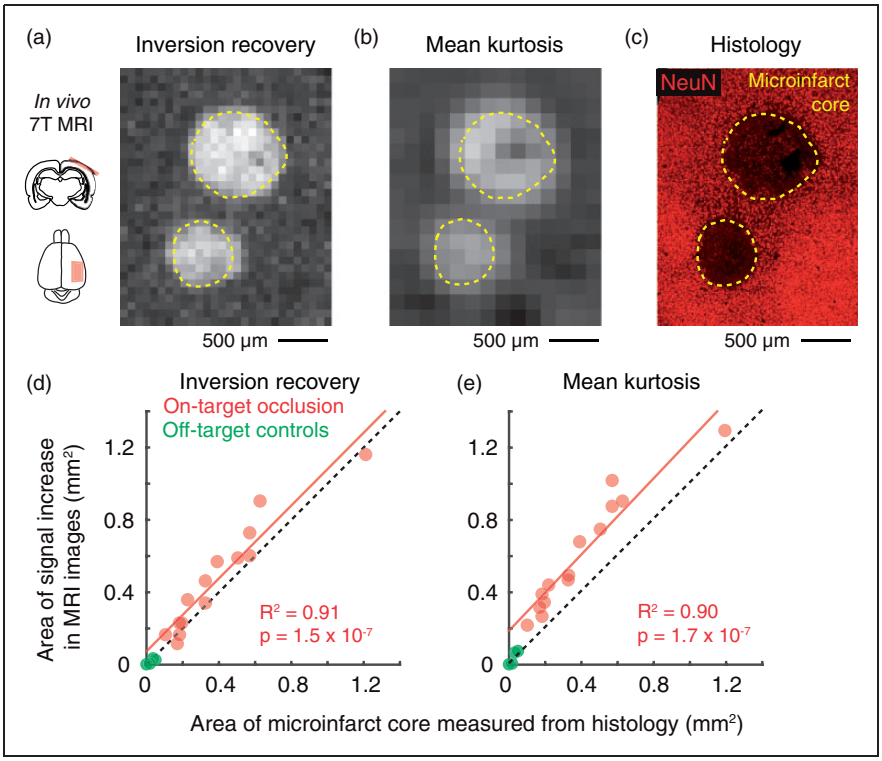

Figure 3. MRI reports the acute microinfarct core. (a,b) IR and MK image of two microinfarcts 24 h after penetrating vessel occlusion. The upper and lower microinfarcts have resulted from arteriole and venular occlusions, respectively. (c) Mice were sacrificed for post-mortem histology immediately following MRI. NeuN staining was performed to identify the extent of the microinfarct core (yellow dotted line). (d, e) Scatterplot of microinfarct area measured in histology versus area of the same microinfarct measured in vivo with IR ($p = 1.5 \times 10^{-7}$, $R^2 = 0.91$; Pearson's correlation) or DKI ($p = 1.7 \times 10^{-7}$, $R^2 = 0.90$; Pearson's correlation). Data are from n = 8 penetrating arteriole and n = 6 penetrating venule occlusions over eight mice. Green data points correspond to microinfarcts generated by off-target control irradiations.

Microinfarcts induce neural deficits throughout peri-lesional tissues

To examine whether microinfarcts impaired the function of peri-lesional tissues, studies were performed with a whisker-to-barrel cortex stimulation assay on awake, head-fixed mice. In animals without an induced microinfarct, stimulation of the whiskers with air puffs led to broad neuronal activation in the contralateral barrel cortex of the primary somatosensory system. This could be detected histologically by immunostaining for c-Fos, an immediate early gene that is rapidly expressed during increased neural activity (Supplementary Figure 2(a) and (b)).[29] In comparison, lower levels of c-Fos were detected in the unstimulated ipsilateral barrel cortex (Supplementary Figure 2(a) and (b)). Expression of NeuN, which is not modulated by neuronal activity, remained unchanged (Supplementary Figure 2(c)). Similarly, expression of the synaptic vesicular glutamate transporter 2 (VGlut2), which demarcates the boundaries of the whisker barrels, was unchanged (Supplementary Figure 2(d)). The advantage of this c-Fos assay was that the entirety of the barrel field could be observed within a single brain slice, allowing the spatial extent of neural impairments to be examined over broad regions of cortex.

We strategically induced penetrating arteriole microinfarcts (or off-target irradiations) at the edge of the barrel cortex such that their impact on c-Fos expression across the barrel field could be examined (Figure 4(a) to (c) and Supplementary Figure 3). At the acute timeframe of three days post-onset, we detected a broad depression of c-Fos expression that extended a radius of 700 µm beyond the microinfarct core, while the core itself averaged only 192 ± 58 µm in radius (Figure 4(d); red). Assuming that neural deficits extended into other cortical layers impacted by the microinfarct column, we estimate the surrounding region of depression to occupy a volume ~12-fold larger than the microinfarct core. Further, layer 4, where c-Fos was examined, is the first to receive input from thalamic projections.[41,42] Therefore, other cortical layers 2/3 and 5, which receive

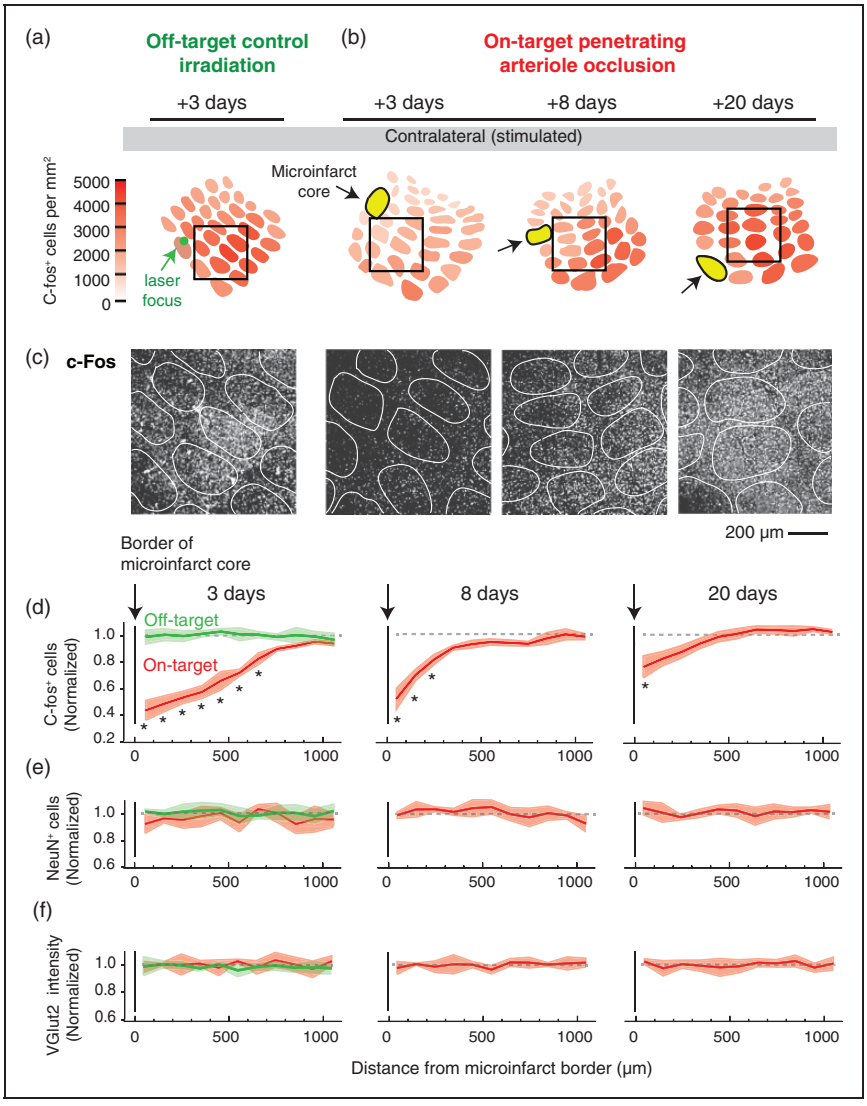

Figure 4. Disruption of neural activity in the peri-lesional tissues surrounding microinfarcts. (a, b) Focal photothrombosis is targeted away from a penetrating arteriole (green; off-target) or directly atop a penetrating arteriole (red; on-target). C-Fos expression in response to whisker stimulation was examined 3, 8, and 20 days following microinfarct induction. Microinfarcts were strategically placed such that their peri-lesional region overlapped with the primary barrel cortex. (c) Example images of c-Fos staining in barrel cortex. The relative location of each image is shown in insets of panels (a) and (b) (black square, 800 × 800 µm area). (d) The number of c-Fos-positive cells decreased in peri-lesional tissues, with the greatest change in the acute time-frame of three days after occlusion ($p = 0.002$ main effect, $F(1.97,3.93) = 135.6$, one-way ANOVA with repeated measures; $^*p < 0.05$, compared to 1000 µm bin with Tukey post hoc analysis). This decrease in c-Fos is not seen with off-target control irradiations (green). While gradual recovery of activity was observed, persistent deficits were detected eight days ($p = 0.006$ main effect, $F(1.38, 2.76) = 59.73$, one-way ANOVA with repeated measures) and 20 days after onset ($p = 0.006$ main effect, $F(1.67, 3.34) = 34.56$, one-way ANOVA with repeated measures). For all data, c-Fos-positive cell counts were normalized to the averaged cell counts obtained from the barrel cortex of three stimulated, but sham treated C57BL/6 mice (no Rose Bengal but laser irradiation). Data are mean ± SEM. Panels (d) to (f) comprise data from n = 3 mice (each with one penetrating arteriole occlusion) for each post-occlusion time-point and the off-target control. (e, f) No change in NeuN-positive cell number or VGlut2 intensity was detected in peri-lesional tissues. Data is mean ± SEM.

downstream input from layer 4, should also exhibit attenuated activity.

Depression of activity in peri-lesional tissues remained prominent for one week, but recovered gradually until c-Fos expression largely reached pre-occlusion levels by three weeks post-onset. No decrease of c-Fos expression was detected with off-target irradiations, confirming that the effect was also not due to the nonspecific actions of photosensitization (Figure 4(d) green). Change in c-Fos expression was not due to commensurate reduction in neuronal numbers, as NeuN staining remained largely unchanged (Figure 4(e)).

This does not indicate, however, that peri-lesional tissues harbor perfectly healthy neurons, as unhealthy but viable neurons may continue to express NeuN.[43,44]

Synaptic changes in peri-lesional tissues

Past studies of microinfarcts (and related small cortical infarcts) in rodents have provided histological evidence for neuronal pathology in peri-lesional tissues. This includes observations of scattered neuronal cell death[11,14] as well as axonal and dendritic damage.[12–14,45] We reasoned that synaptic loss should also correlate with peri-lesional deficits. VGlut2 immunostaining has been shown to be sensitive to changes in synaptic density, as staining is profoundly decreased in tissues affected by large-scale stroke.[46] Unexpectedly, VGlut2 staining intensity was unaffected in peri-lesional tissues in all post-onset time-points examined (Figure 4(f)). To provide a second measure of synaptic protein content, we stained for synaptophysin in another cohort of mice, sacrificed at two days post-occlusion ($n = 3$) (Supplementary Figure 8). Synaptophysin was consistent with VGlut2 data, showing no decrease in peri-lesional tissues. We then obtained more sensitive measurements of synaptic change by directly measuring dendritic spine densities of individual layer 2/3 excitatory neurons in Thy1-YFP-H mice (Figure 5(a) to (d)).[47] Spine density of neurons within the peri-lesional zone was, on average, 25% lower than neurons more distant from the microinfarct core (Figure 5(e) and (f)). Blebbing and thinning of dendrites were also evident nearer the microinfarct core (Figure 5(d)). These data indicate that microinfarcts disrupt neuronal synapses in surrounding tissues. However, immunostaining for some presynaptic proteins may not adequately report this change.

Microinfarcts cause persistent disruption of hemodynamics in peri-lesional tissues

In the normal brain, neuronal activity is strongly coupled to an increase in local blood flow in order to meet the high metabolic demand of neural processing. Thus, microinfarct-induced disruption of neural activity or neurovascular coupling should also depress the hemodynamic response *in vivo*. We examined this possibility by imaging sensory-evoked dilation of pial arterioles in awake, head-fixed mice using two-photon microscopy (Figure 6(a)).[26] Microinfarcts were again placed strategically at the edge of the barrel cortex (Figure 6(b)). Consistent with c-Fos data (Figure 4), we observed a pronounced reduction of dilatory activity in response to whisker stimulation at ~3 days post occlusion, which recovered only partially over the following two weeks (Figure 6(c)). Critically, a loss of arteriole dilation was also observed well beyond the microinfarct core (Figure 7(a) to (c); red). Pial surface arterioles and penetrating arterioles were affected similarly (Figure 7(a) to (c); open vs. filled red circles, respectively). In contrast, no disturbance in hemodynamic function was seen with the off-target irradiation (Figure 7(a); green). In separate cohorts of mice, hemodynamic responses were found to decrease within 3 h following the occlusive event, indicating rapid development of impairment following penetrating arteriole occlusion (Supplementary Figure 9). Further, mice receiving sham occlusions (penetrating arteriole irradiation but no Rose Bengal) did not exhibit reduction in hemodynamic function, suggesting that these changes were not a result of animal preparation, repeated imaging, or exposure to green laser light (Supplementary Figure 10).

We quantified hemodynamic function over all post-occlusion time-points examined and found that response magnitude was 20% of pre-occlusion levels at 2 to 3 days after microinfarct onset (Figure 7(d)). Despite some recovery, response magnitude remained at ~70% of pre-occlusion levels for over two weeks. We also detected a lag in the latency to dilation that persisted for at least one week (Figure 7(e)), particularly in arterioles closer to the microinfarct core (Supplementary Figure 11). Hemodynamic lags have been reported for large human strokes and may be due to disruption of neural firing, neurovascular coupling or changes in vascular wall compliance.[48] The average baseline diameters of pial arterioles did not differ between imaging time-points, suggesting that loss of dilative capacity was not because arterioles were already maximally dilated (Figure 7(f)). A small increase in baseline arteriole diameter was detected at 14–17 days post-occlusion, possibly due to chronic vascular remodeling.[49] Critically, arterioles retained the ability to dilate in response to inhalation of isoflurane, an anesthetic with potent vasodilatory properties (Figure 7(f)); only a modest but significant decrease in isoflurane-induced vasodilation was detected at 2 to 3 and 7 to 9 days post-occlusion. This suggested that a dysfunction in neurons or neurovascular coupling was the primary reason for peri-lesional deficits, and that loss of compliance in the vascular wall, i.e. vascular stiffening, was minor (Figure 7(g)).

Peri-lesional deficits are insufficiently detected by MRI

We next examined whether peri-lesional impairments were associated with change in microstructural heterogeneity that allowed it to be discerned from normal tissue using MRI. MK was measured from core and peri-lesional regions of six arteriole microinfarcts

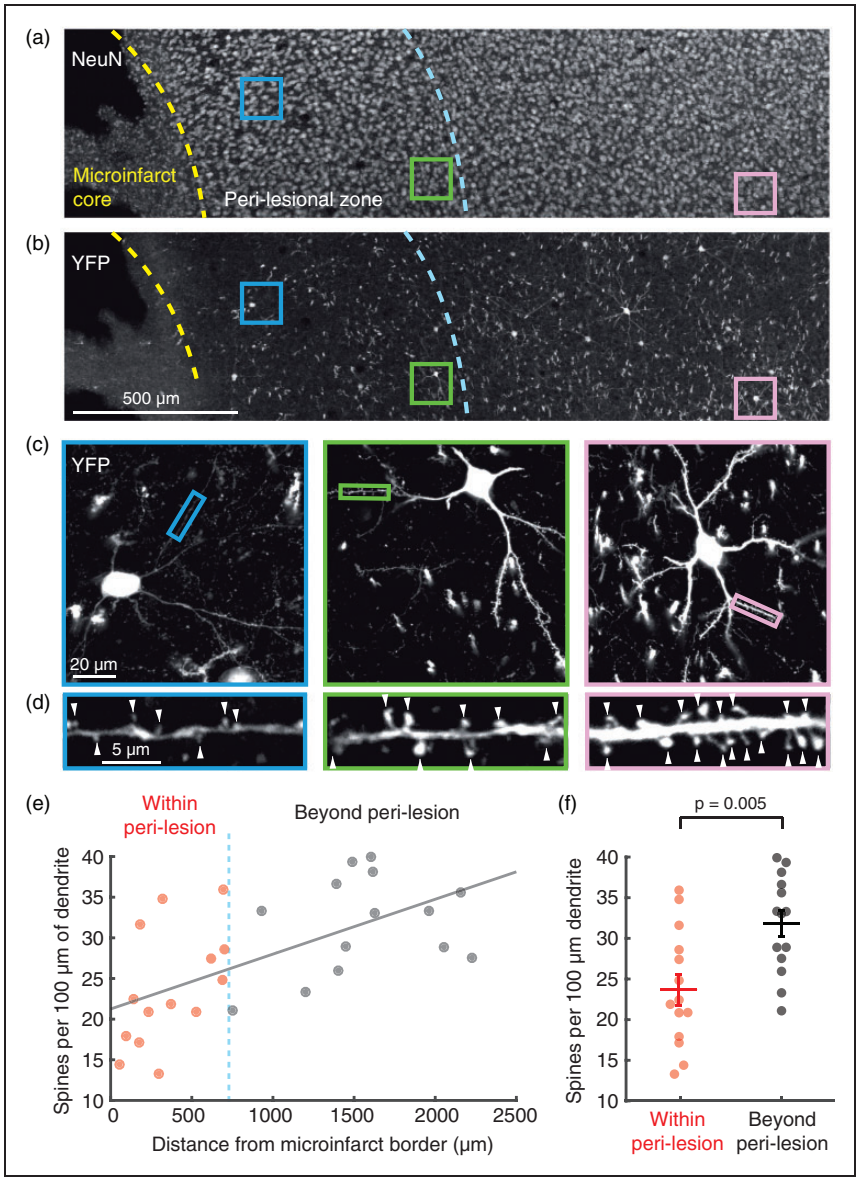

Figure 5. Dendritic spine density is decreased in peri-lesional tissues. (a) Two days post-occlusion, absence of NeuN staining demarcates the microinfarct core, the border of which is traced with a yellow dashed line. Viable neurons exist beyond the microinfarct core, evidenced by robust NeuN staining, but C-fos studies in Figure 4 demonstrated functional deficits up to 700 um beyond the core (blue dashed line). (b) In the same slice, YFP brightly labels layer 2/3 cortical neurons and their processes. Colored squares highlight example YFP and NeuN-positive pyramidal neurons that were selected for high resolution imaging of dendrites. (c) High resolution confocal microscopy of dendrites. Images shown are 30 µm average intensity projections. Small colored rectangles indicate a typical dendritic segment used for spine counting. (d) Individual spines were manually counted along isolated dendritic segments (arrowheads), and divided by the length of dendritic segment analyzed to provide a measure of spine density. An average spine density for each neuron (n = 28 neurons in total) was calculated from several dendritic segments. (e) Mean spine density per neuron versus the neuron's distance from the microinfarct core. Spine density decreases closer to the microinfarct core (Pearson, $R^2 = 0.38$, $p = 0.0005$). (f) Cells within the peri-lesional region show a significant ~25% decrease in spine density compared to cells beyond the peri-lesional region (n = 14 neurons/group compiled over two mice, $p = 0.005$ by Wilcoxon Rank-sum test). Data are mean ± SEM.

generated in three mice that were comparable in size and location to those induced for c-Fos assays or two-photon imaging of hemodynamics (Figure 8(a) and (b)). In these experiments, MRI voxel dimensions were modified to cover a broader depth of cortex, i.e. $0.078 \times 0.078 \times 0.5$ (depth) mm^3 versus $0.2 \times 0.2 \times 0.3$ (depth) mm^3 for previous scans, to capture potential changes in cortical layer 4 where the whisker barrels reside. While MK within the core exhibited robust increase (Figure 8(c)), we detected no change

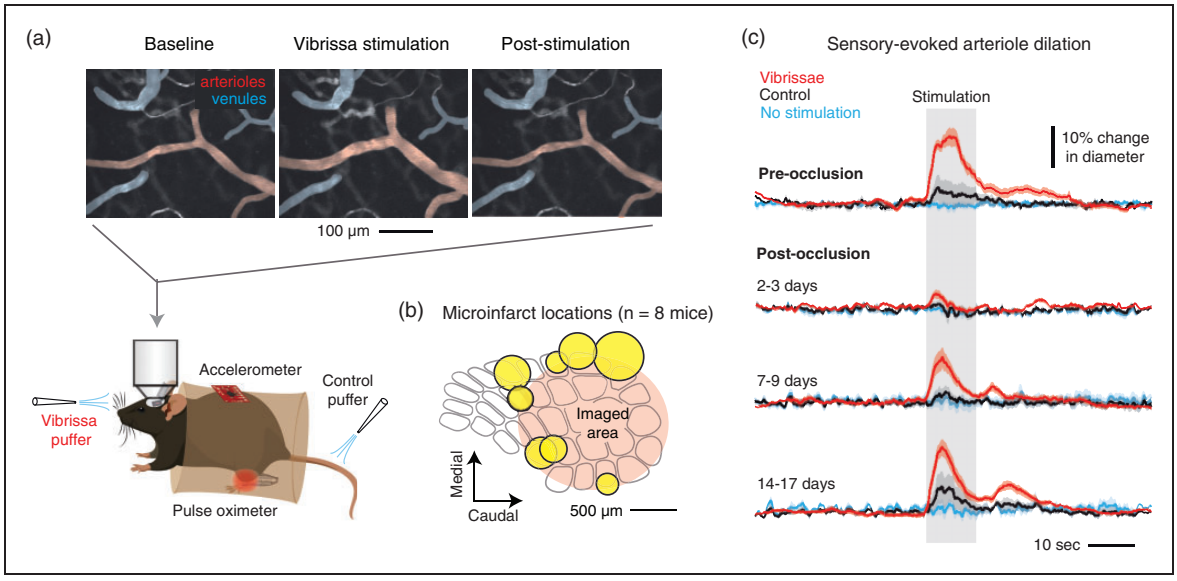

Figure 6. Arteriole reactivity following strategic placement of microinfarcts in barrel cortex. (a) Awake, head-fixed mice were imaged with two-photon microscopy to examine pial and penetrating arteriole dilation in response to whisker stimulation, i.e. functional hyperemia. As a control for general arousal, air puffs were delivered to the tail. (b) In each mouse (n = 8), a single microinfarct was strategically placed to flank the primary barrel cortex. The positions of all eight microinfarcts (yellow) are shown as a composite. (c) Sensory-evoked arteriole dilation pre-occlusion and at various periods following penetrating arteriole occlusion. N = 36 arterioles (15 surface arterioles, 21 penetrating arterioles) over eight mice. Data are mean ± SEM.

in peri-lesional tissues when functional deficits were most severe at one to three days post-occlusion (Figure 8(d)). A modest but significant MK increase of 15% was detected at seven days post-occlusion in peri-lesional regions, which may have reflected the delayed astroglial response that we observed histologically (Figure 2(d)). Overall, this analysis suggested that peri-lesional changes associated with functional impairment were largely invisible to MRI, though the delayed response to this pathology can lead to small but consistent changes in tissue microstructure.

Discussion

Here we used a preclinical model to examine how individual cortical microinfarcts impact the function of surrounding tissues over a period of several weeks after onset (Figure 8(e)). Using ex vivo c-Fos immunostaining and *in vivo* two-photon imaging of single-vessel hemodynamics to assess brain function, our key finding was that sensory-evoked neural activity was significantly diminished beyond the microinfarct core, with an estimated volume of impaired cortical tissues at least 12-fold larger than the lesion core itself. Further, sensory-evoked hemodynamics remained partially depressed for 14–17 days post-occlusion suggesting that these widespread deficits are also long-lasting. In contrast to the hemodynamic responses, sensory-evoked c-Fos expression in the peri-lesion recovered in later stages of injury, but this apparent dissociation from hemodynamic responses may be because c-Fos does not adequately report a partial loss of neural activity, or that neurovascular coupling remained disrupted. Overall, however, our results support the conclusion that microinfarcts cause persistent attenuation of neuronal activity and/or neurovascular coupling over a cortical area larger than the lesion core.[4] Finally, we show that *in vivo* MRI is able to detect the acute/subacute pathology occurring within the microinfarct core, but does not adequately report pathophysiological changes in the peri-lesional tissues.

How might the peri-lesional effects of microinfarcts be relevant to VCID? First, the collective dysfunction resulting from hundreds to thousands of microinfarcts is significantly greater than can be surmised through routine radiological or histological examinations. This "invisible" pathology occurring beyond the microinfarct core may contribute to long-term damage or disorganization of brain circuitry. Second, our detection of persistent functional deficits suggests that microinfarct contributions to VCID may be lasting and cumulative. Third, microinfarcts may contribute to lowering the threshold for cognitive impairment in individuals with co-existing Alzheimer's disease pathology.[5] For example, peri-lesional neurons or vasculature may be more susceptible to Aβ toxicity. Impairment of hemodynamics and chronic astrogliosis could lead to reduced Aβ clearance.[50,51]

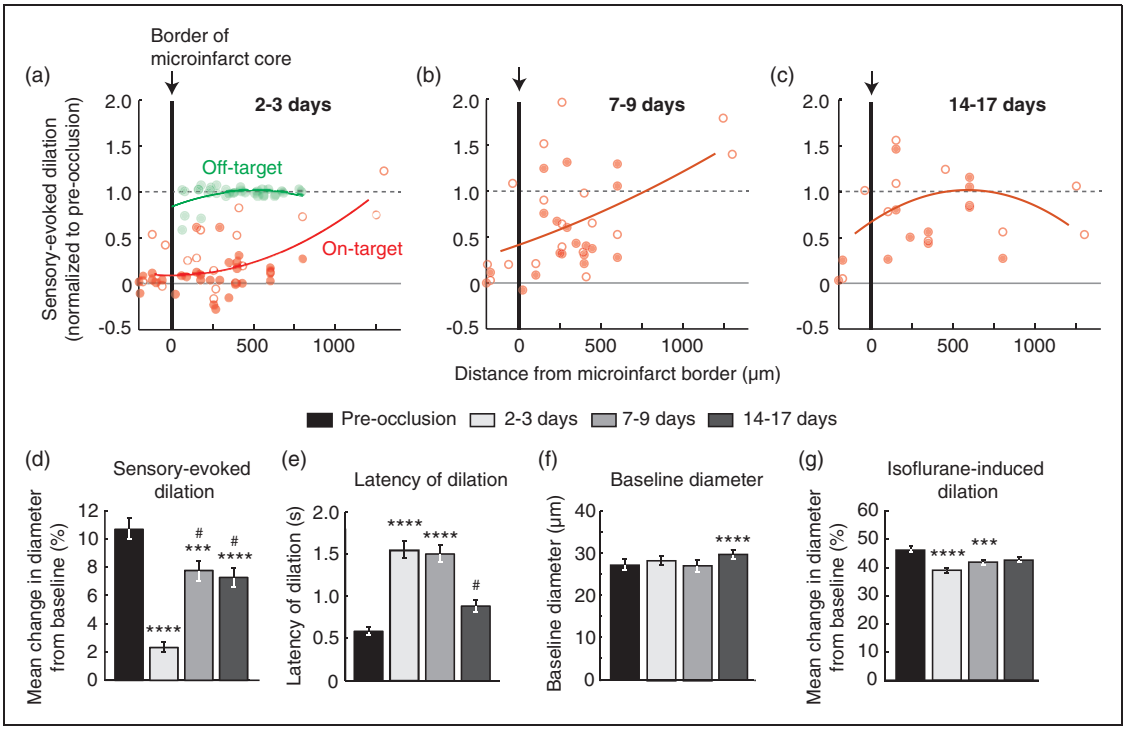

Figure 7. Disruption of single-vessel hemodynamics in peri-lesional tissues surrounding microinfarcts. (a–c) Sensory-evoked dilation as a function of distance from the microinfarct core (red; n = 50, 36, and 24 arterioles over six mice for panels a, b, and c, respectively). Open circles represent surface arterioles, and filled circles represent penetrating arterioles. An off-target control group showed no change in dilatory function beyond the region of photothrombotic irradiation (green in panel a; n = 33 arterioles over three mice). Lines correspond to second order polynomial regression fits of the data. (d) Mean change in diameter during whisker stimulation over a group of arterioles that could be measured repeatedly over all time-points ($p < 0.0001$ main effect, Friedman statistic = 82.1, Friedman test with repeated measures; Dunn's post hoc yields $^{****}p < 0.0001$ or $^{***}p < 0.001$, compared to pre-occlusion, and $^{\#}p < 0.05$, compared to 2 to 3 days; n = 36 arterioles over six mice). Data are mean ± SEM. (e) Latency to peak dilation after onset of stimulation ($p < 0.0001$ main effect, Friedman statistic = 82.6, Friedman test with repeated measures; Dunn's post hoc yields $^{****}p < 0.0001$, compared to pre-occlusion, and $^{\#}p < 0.05$, compared to 2 to 3 days and 7 to 9 days). (f) Baseline diameter of arterioles prior to stimulation. ($p < 0.0001$ main effect, F(2.42,84.58) = 8.96, one-way ANOVA with repeated measures; Tukey's post hoc yields $^{****}p < 0.0001$, compared to pre-occlusion). (g) Mean change in diameter after inhalation of vasodilating anesthetic isoflurane (3% MAC in air) ($p < 0.0001$ main effect, Friedman statistic = 39.9, Friedman test with repeated measures; Dunn's post hoc yields $^{****}p < 0.0001$ or $^{***}p < 0.001$, compared to pre-occlusion).

There is some evidence for peri-lesional changes associated with microinfarcts in the human brain. The most common reports are of diffuse fibrillary gliosis beyond the microinfarct core.[52] While astrogliosis can be beneficial with its roles in wound closure and blood–brain barrier repair, it can also elicit pro-inflammatory cascades and interfere with synaptic growth.[53] Interestingly, in a mouse model of distributed microinfarcts,[14] the polarity of the astrocytic water channel, aquaporin 4, was abnormal, which may be detrimental since this protein is required for glymphatic clearance.[54] With respect to neurons, Hinman et al.[55] examined human white matter microinfarcts and found molecular disorganization of axons and myelin at substantial distances from the microinfarct core, an effect that likely disrupted axon conduction. In future work, it will be important to identify additional molecular targets for immunostaining that can reveal peri-lesional damage caused by microinfarcts. A cautionary note from this study is that markers for presynaptic proteins (synaptophysin and VGlut2) and neuronal viability (NeuN) failed to report peri-lesional regions, despite observations of dendritic spine loss in Thy1-YFP mice. Thus, neurodegeneration and functional impact may be in better agreement when more sensitive markers for neuronal decline are used.

A number of plausible mechanisms could underlie the observed functional deficits. One possibility is the occurrence of ischemic cortical spreading depression (CSD),[56,57] which we previously demonstrated in a rat model of single penetrating vessel occlusion.[11] CSD waves are intense depolarizations that can propagate for many millimeters beyond the core, leading to excessive excitatory neurotransmitter release and potentially

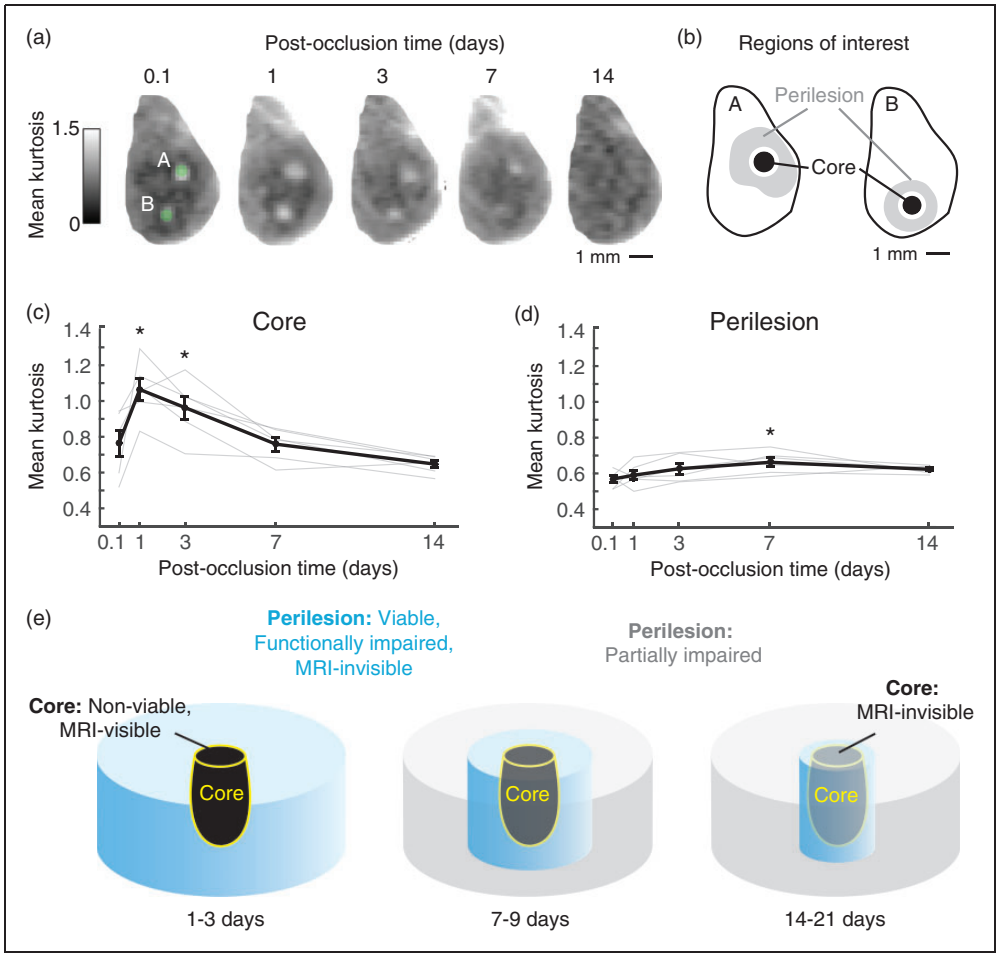

Figure 8. Core versus peri-lesional changes and relation to MRI signal. (a) Two arteriole microinfarcts imaged with DKI over a span of 14 days post-occlusion. (b) MK was quantified in core and peri-lesional regions. The regions of interest were selected from a time-point of peak microinfarct visibility (typically one day post-occlusion) and applied to all other time-points. See Materials and Methods for additional details. (c) MK of the microinfarct core plotted as a function of post-occlusion time ($p = 0.0001$ main effect, $F(4, 20) = 15.86$, one-way ANOVA with repeated-measures; Tukey post hoc yields $^*p < 0.05$, compared to 0.1, 7, and 14 days; $n = 6$ arteriole microinfarcts over three mice). Data = mean ± SEM. (d) Mean kurtosis of peri-lesional tissues for the same microinfarcts plotted as a function of post-occlusion time. ($^*p = 0.02$ main effect, $F(4, 20) = 3.59$, one-way ANOVA with repeated-measures; Tukey post hoc yields $^*p < 0.05$, compared to 0.1 day). Data = mean ± SEM. (e) Evolution of acute microinfarct pathology. At 1–3 days post-occlusion, the non-viable core is visible to both structural (T2/IR) and diffusion MRI. Peri-lesional tissues remain viable, but are functionally impaired and insufficiently detected by MRI. At 7–9 days, the core is detectable only to diffusion MRI. The peri-lesional tissues begin to recover in function, and show a modest increase in MK relative to earlier time-points. At 14–21 days, the core is no longer visible to MRI, and peri-lesional tissues exhibit only partial responsiveness to sensory input.

lasting damage to fine neuronal structure.[58] While CSD has been well studied in large-scale stroke,[59,60] their role in microinfarct injury remains poorly understood. Another potential mechanism is diaschisis, where death of neurons within the core disables the cortical and subcortical circuits to which they were previously integrated.[61] For example, small infarcts generated in motor cortex also cause widespread impairment beyond the lesion core.[62] However, this impairment was not due to an inability to excite cortical neurons, but rather a blockade of motor output through subcortical relays that lie far from the lesion core. Finally, studies have also shown that excessive inhibitory tone is involved in depressing activity in peri-infarct tissues, a mechanism that is attributed to increased extrasynaptic GABAergic neurotransmission and reduced GABA uptake.[63] Future studies are needed to determine which of these mechanisms are most important in microinfarct injury.

Recent clinical studies have demonstrated the feasibility of visualizing human microinfarcts with 7T[3,33] and 3 T MRI.[9,64] In addition to facilitating the use of microinfarct signals as a potential MRI biomarker for VCID,[65] longitudinal *in vivo* imaging can provide

information about their chronic effects.[66] Animal models can complement this clinical work by providing additional information on how microinfarct signals evolve. For example, we showed that structural and diffusion MRI are primarily sensitive to the acute microinfarct core, but not to peri-lesional tissues experiencing functional deficit. Further, consistent with recent estimates from human studies, our findings support the idea that acute microinfarcts are only visible for one to two weeks.[4,19] However, clinical studies have shown that some microinfarcts exhibiting neuropathological features of a chronic lesion are visible with ex vivo structural MRI.[35] One possibility for this is that there is a secondary, lasting increase in MRI signal contrast that occurs beyond the time-frame we have studied here. Another possibility is that microinfarcts larger than the ones induced in this study, i.e., >1 mm in diameter, cause greater perturbations of tissue structure that can be seen long-term with MRI, such as the formation of a cyst.

The strength of this study is the ability to precisely induce cortical microinfarcts with respect to location and onset time.[11,23] This proved essential when examining the impact of isolated microinfarcts within the mouse vibrissa sensory system, and when studying their evolution with multimodal MRI.[11,22] Limitations of the study included the use of mice without any risk factors for microinfarcts, i.e. advanced age, or Alzheimer's disease background, which is a goal of future studies. Additionally, we have modeled only a subset of human cortical microinfarcts that are continuous with the pial surface, and not those confined within the cortex that likely result from obstruction of deeper penetrating arterioles branches.[16] Finally, this study has focused on cortical changes. In future work, it will be important to understand whether microinfarcts impair the function of remote brain regions by damaging white matter fibers tracts.

Funding

The author(s) disclosed receipt of the following financial support for the research, authorship, and/or publication of this article: This work was funded by grants to A.Y.S. from the NINDS (NS085402), the Dana Foundation, South Carolina Clinical and Translational Institute (UL1TR000062), and an Institutional Development Award (IDeA) from the NIGMS under grant number P20GM12345. DAH. is supported by the MUSC MSTP (NIH T32 GM08716), the South Carolina Clinical & Translational Research (SCTR) Institute, (NIH – NCATS UL1 TR001450 and NIH – NCATS TL1 TR001451), and an F30 award (1F30NS096868).

Acknowledgements

We thank Susanne van Veluw and Geert Jan Biessels for allowing use of their images and critical reading the manuscript. We also thank Patrick J Drew for providing analysis code, Andrée-Anne Berthiaume for reading the manuscript, and Zachary J Taylor for technical assistance. We are grateful to David Kleinfeld and Steven M. Greenberg for helpful discussions.

Declaration of conflicting interests

The author(s) declared no potential conflicts of interest with respect to the research, authorship, and/or publication of this article.

Authors' contributions

AYS, ESH, XN ETM RLD, JAH, and JHJ designed, executed, and analyzed the MRI studies PMS, DAH, and AYS designed, executed and analyzed the two-photon imaging studies, and histological studies. AYS wrote the manuscript with feedback from all other authors.

Supplementary material

Supplementary material for this paper can be found at http://journals.sagepub.com/doi/suppl/10.1177/0271678X16685573

References

1. Gorelick PB, Scuteri A, Black SE, et al. Vascular contributions to cognitive impairment and dementia: A statement for healthcare professionals from the American Heart Association/American Stroke Association. *Stroke* 2011; 42: 2672–713.
2. Iadecola C. The pathobiology of vascular dementia. *Neuron* 2013; 80: 844–866.
3. Brundel M, de Bresser J, van Dillen JJ, et al. Cerebral microinfarcts: A systematic review of neuropathological studies. *J Cereb Blood Flow Metab* 2012; 32: 425–436.
4. Smith EE, Schneider JA, Wardlaw JM, et al. Cerebral microinfarcts: The invisible lesions. *Lancet Neurol* 2012; 11: 272–282.
5. Kapasi A and Schneider JA. Vascular contributions to cognitive impairment, clinical Alzheimer's disease, and dementia in older persons. *Biochim Biophys Acta* 2016; 1862: 878–886.
6. Arvanitakis Z, Leurgans SE, Barnes LL, et al. Microinfarct pathology, dementia, and cognitive systems. *Stroke* 2010; 42: 722–727.
7. Kövari E, Gold G, Herrmann FR, et al. Cortical microinfarcts and demyelination affect cognition in cases at high risk for dementia. *Neurology* 2007; 66: 927–931.
8. Launer LJ, Hughes TM and White LR. Microinfarcts, brain atrophy, and cognitive function: The Honolulu Asia Aging Study Autopsy Study. *Ann Neurol* 2011; 70: 774–780.
9. van Dalen JW, Scuric EE, van Veluw SJ, et al. Cortical microinfarcts detected *in vivo* on 3 Tesla MRI: Clinical and radiological correlates. *Stroke* 2015; 46: 255–257.
10. van Rooden S, Goos JD, van Opstal AM, et al. Increased number of microinfarcts in Alzheimer disease at 7-T MR imaging. *Radiology* 2014; 270: 205–211.

11. Shih AY, Blinder P, Tsai PS, et al. The smallest stroke: Occlusion of one penetrating vessel leads to infarction and a cognitive deficit. *Nat Neurosci* 2013; 16: 55–63.
12. Rapp JH, Pan XM, Neumann M, et al. Microemboli composed of cholesterol crystals disrupt the blood-brain barrier and reduce cognition. *Stroke* 2008; 39: 2354–2361.
13. Silasi G, She J, Boyd JD, et al. A mouse model of small-vessel disease that produces brain-wide-identified micro-occlusions and regionally selective neuronal injury. *J Cereb Blood Flow Metab* 2015; 35: 734–738.
14. Wang M, Iliff JJ, Liao Y, et al. Cognitive deficits and delayed neuronal loss in a mouse model of multiple microinfarcts. *J Neurosci* 2012; 32: 17948–17960.
15. Arvanitakis Z, Capuano AW, Leurgans SE, et al. The relationship of cerebral vessel pathology to brain micro-infarcts. *Brain Pathol* 2016; in press.
16. Zheng L, Vinters HV, Mack WJ, et al. Cerebral atherosclerosis is associated with cystic infarcts and microinfarcts but not Alzheimer pathologic changes. *Stroke* 2013; 44: 2835–2841.
17. Okamoto Y, Yamamoto T, Kalaria RN, et al. Cerebral hypoperfusion accelerates cerebral amyloid angiopathy and promotes cortical microinfarcts. *Acta Neuropathol* 2012; 123: 381–394.
18. Westover MB, Bianchi MT, Yang C, et al. Estimating cerebral microinfarct burden from autopsy samples. *Neurology* 2013; 80: 1365–1369.
19. Auriel E, Westover MB, Bianchi MT, et al. Estimating total cerebral microinfarct burden from diffusion-weighted imaging. *Stroke* 2015; 46: 2129–2135.
20. Sonnen JA, Larson EB, Crane PK, et al. Pathological correlates of dementia in a longitudinal, population-based sample of aging. *Ann Neurol* 2007; 62: 406–413.
21. van Veluw SJ, Hilal S, Kuijf HJ, et al. Cortical microinfarcts on 3T MRI: Clinical correlates in memory-clinic patients. *Alzheimers Dement* 2015; 11: 1500–9.
22. Taylor ZJ, Hui ES, Watson AN, et al. Microvascular basis for growth of small infarcts following occlusion of single penetrating arterioles in mouse cortex. *J Cereb Blood Flow Metab* 2016; 36: 1357–1373.
23. Shih AY, Driscoll JD, Drew PJ, et al. Two-photon microscopy as a tool to study blood flow and neurovascular coupling in the rodent brain. *J Cereb Blood Flow Metab* 2012; 32: 1277–1309.
24. Drew PJ, Shih AY, Driscoll JD, et al. Chronic optical access through a polished and reinforced thinned skull. *Nat Meth* 2010; 7: 981–984.
25. Masamoto K and Kanno I. Anesthesia and the quantitative evaluation of neurovascular coupling. *J Cereb Blood Flow Metab* 2012; 32: 1233–1247.
26. Drew PJ, Shih AY and Kleinfeld D. Fluctuating and sensory-induced vasodynamics in rodent cortex extends arteriole capacity. *Proc Natl Acad Sci U S A* 2011; 108: 8473–8478.
27. Taylor ZJ and Shih AY. Targeted occlusion of individual pial vessels of mouse cortex. *Bio Protoc* 2013; 3: e897.
28. Tabesh A, Jensen JH, Ardekani BA, et al. Estimation of tensors and tensor-derived measures in diffusional kurtosis imaging. *Magn Reson Med* 2011; 65: 823–836.
29. Lecrux C, Toussay X, Kocharyan A, et al. Pyramidal neurons are ''neurogenic hubs'' in the neurovascular coupling response to whisker stimulation. *J Neurosci* 2011; 31: 9836–9847.
30. Blinder P, Tsai PS, Kaufhold JP, et al. The murine cortical angiome: An interconnected vascular network with noncolumnar patterns of blood flow. *Nat. Neurosci* 2013; 16: 889–897.
31. Soontornniyomkij V, Lynch MD, Mermash S, et al. Cerebral microinfarcts associated with severe cerebral beta-amyloid angiopathy. *Brain Pathol* 2010; 20: 459–467.
32. Nishimura N, Schaffer CB, Friedman B, et al. Penetrating arterioles are a bottleneck in the perfusion of neocortex. *Proc Natl Acad Sci U S A* 2007; 104: 365–370.
33. van Veluw SJ, Zwanenburg JJ, Engelen-Lee J, et al. *In vivo* detection of cerebral cortical microinfarcts with high-resolution 7T MRI. *J Cereb Blood Flow Metab* 2013; 33: 322–329.
34. Sofroniew MV and Vinters HV. Astrocytes: Biology and pathology. *Acta Neuropathol* 2010; 119: 7–35.
35. van Veluw SJ, Zwanenburg JJ, Rozemuller AJ, et al. The spectrum of MR detectable cortical microinfarcts: A classification study with 7-tesla postmortem MRI and histopathology. *J Cereb Blood Flow Metab* 2015; 35: 676–683.
36. Lerch JP, Carroll JB, Dorr A, et al. Cortical thickness measured from MRI in the YAC128 mouse model of Huntington's disease. *Neuroimage* 2008; 41: 243–251.
37. Im K, Lee JM, Seo SW, et al. Variations in cortical thickness with dementia severity in Alzheimer's disease. *Neurosci Lett* 2008; 436: 227–231.
38. Lauwers F, Cassot F, Lauwers-Cances V, et al. Morphometry of the human cerebral cortex microcirculation: General characteristics and space-related profiles. *Neuroimage* 2008; 39: 936–948.
39. Jensen JH, Helpern JA, Ramani A, et al. Diffusional kurtosis imaging: The quantification of non-gaussian water diffusion by means of magnetic resonance imaging. *Magn Reson Med* 2005; 53: 1432–1440.
40. Hui ES, Du F, Huang S, et al. Spatiotemporal dynamics of diffusion kurtosis, mean diffusivity and perfusion changes in experimental stroke. *Brain Res* 2012; 1451: 100–109.
41. Fox K. *Barrel cortex*. Cambridge: Cambridge University Press, 2008.
42. Petersen CC. The functional organization of the barrel cortex. *Neuron* 2007; 56: 339–355.
43. Unal-Cevik I, Kilinç M, Gürsoy-Ozdemir Y, et al. Loss of NeuN immunoreactivity after cerebral ischemia does not indicate neuronal cell loss: A cautionary note. *Brain Res* 2004; 1015: 169–174.
44. Liu F, Schafer DP and McCullough LD. TTC, fluoro-Jade B and NeuN staining confirm evolving phases of infarction induced by middle cerebral artery occlusion. *J Neurosci Meth* 2009; 170: 1–8.

45. Enright LE, Zhang S and Murphy TH. Fine mapping of the spatial relationship between acute ischemia and dendritic structure indicates selective vulnerability of layer V neuron dendritic tufts within single neurons *in vivo*. *J Cereb Blood Flow Metab* 2007; 27: 1185–1200.
46. Sánchez-Mendoza E, Burguete MC, Castelló-Ruiz M, et al. Transient focal cerebral ischemia significantly alters not only EAATs but also VGLUTs expression in rats: Relevance of changes in reactive astroglia. *J Neurochem* 2010; 113: 1343–1355.
47. Feng G, Mellor RH, Bernstein M, et al. Imaging neuronal subsets in transgenic mice expressing multiple spectral variants of GFP. *Neuron* 2000; 28: 41–51.
48. Siegel JS, Snyder AZ, Ramsey L, et al. The effects of hemodynamic lag on functional connectivity and behavior after stroke. *J Cereb Blood Flow Metab* 2016; 36: 2162–2176.
49. Coyle P. Diameter and length changes in the cerebral collaterals after middle cerebral artery occlusion in the young rat. *Anat Rec* 1984; 210: 357–364.
50. Iliff JJ, Wang M, Zeppenfeld DM, et al. Cerebral arterial pulsation drives paravascular CSF-interstitial fluid exchange in the murine brain. *J Neurosci* 2013; 33: 18190–18199.
51. Garcia-Alloza M, Gregory J, Kuchibhotla KV, et al. Cerebrovascular lesions induce transient β-amyloid deposition. *Brain* 2011; 134: 3697–3707.
52. Vinters HV, Ellis WG, Zarow C, et al. Neuropathologic substrates of ischemic vascular dementia. *J Neuropath Exp Neurol* 2000; 59: 931–945.
53. Sofroniew MV. Astrocyte barriers to neurotoxic inflammation. *Nat Rev Neurosci* 2015; 16: 249–263.
54. Iliff JJ, Wang M, Liao Y, et al. A paravascular pathway facilitates CSF flow through the brain parenchyma and the clearance of interstitial solutes, including amyloid β. *Sci Transl Med* 2012; 4: 147ra11.
55. Hinman JD, Lee MD, Tung S, et al. Molecular disorganization of axons adjacent to human lacunar infarcts. *Brain* 2015; 138: 736–745.
56. von Bornstädt D, Houben T, Seidel JL, et al. Supply-demand mismatch transients in susceptible peri-infarct hot zones explain the origins of spreading injury depolarizations. *Neuron* 2015; 85: 1117–1131.
57. Kao YC, Li W, Lai HY, et al. Dynamic perfusion and diffusion MRI of cortical spreading depolarization in photothrombotic ischemia. *Neurobiol Dis* 2014; 71: 131–139.
58. Murphy TH, Li P, Betts K, et al. Two-photon imaging of stroke onset *in vivo* reveals that NMDA-receptor independent ischemic depolarization is the major cause of rapid reversible damage to dendrites and spines. *J Neurosci* 2008; 28: 756–772.
59. Ayata C and Lauritzen M. Spreading depression, spreading depolarizations, and the cerebral vasculature. *Physiol Rev* 2015; 95: 953–993.
60. Somjen GG. Mechanisms of spreading depression and hypoxic spreading depression-like depolarization. *Physiol Rev* 2001; 81: 1065–1096.
61. Carmichael ST, Tatsukawa K, Katsman D, et al. Evolution of diaschisis in a focal stroke model. *Stroke* 2004; 35: 758–763.
62. Anenberg E, Arstikaitis P, Niitsu Y, et al. Ministrokes in channelrhodopsin-2 transgenic mice reveal widespread deficits in motor output despite maintenance of cortical neuronal excitability. *J Neurosci* 2014; 34: 1094–1104.
63. Clarkson AN, Huang BS, Macisaac SE, et al. Reducing excessive GABA-mediated tonic inhibition promotes functional recovery after stroke. *Nature* 2010; 468: 305–309.
64. van Veluw SJ, Hilal S, Kuijf HJ, et al. Cortical microinfarcts on 3T MRI: Clinical correlates in memory-clinic patients. *Alzheimers Dement* 2015; 11: 1500–1509.
65. Wardlaw JM, Smith EE, Biessels GJ, et al. Neuroimaging standards for research into small vessel disease and its contribution to ageing and neurodegeneration. *Lancet Neurol* 2013; 12: 822–838.
66. Auriel E, Edlow BL, Reijmer YD, et al. Microinfarct disruption of white matter structure: A longitudinal diffusion tensor analysis. *Neurology* 2014; 83: 182–188.